Lawrence Berkeley Laboratory
UNIVERSITY OF CALIFORNIA

Materials & Chemical Sciences Division

National Center for Electron Microscopy

Presented at the 44th Annual Meeting of the Electron Microscopy Society of America, Albuquerque, NM, August 10–15, 1986

SPECTROSCOPIC INFORMATION FROM HIGH RESOLUTION IMAGES

R. Gronsky

May 1987

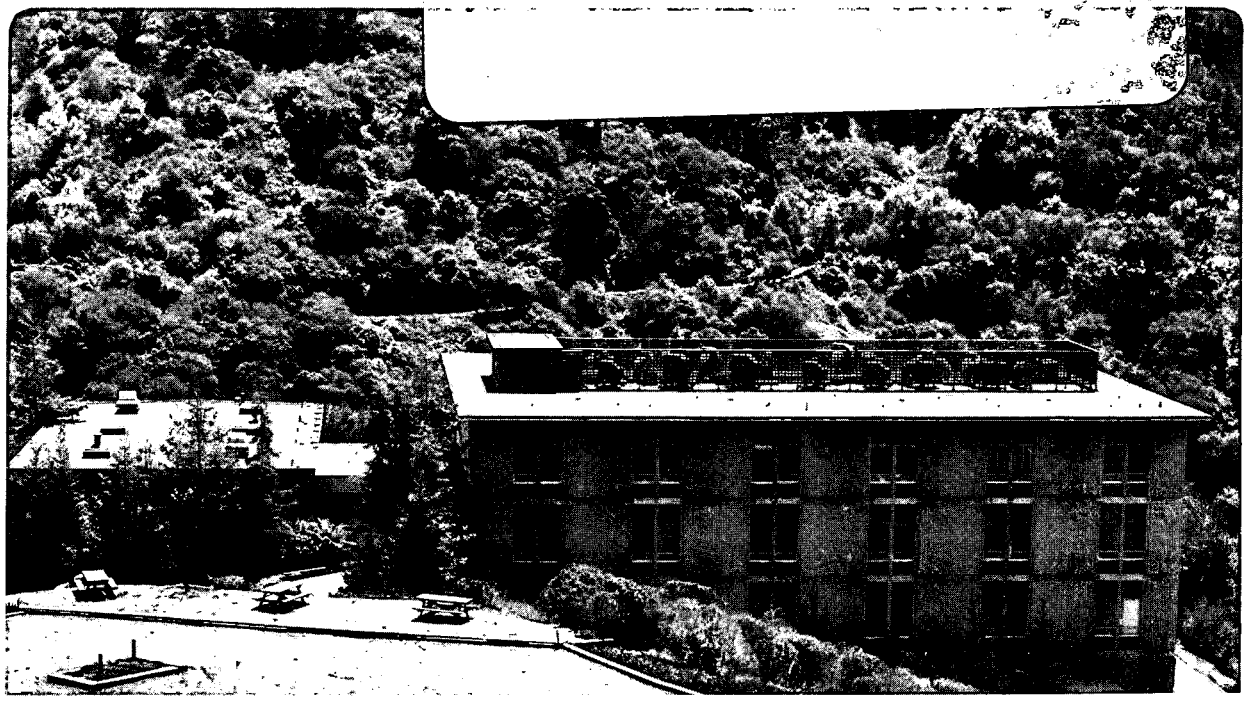

Prepared for the U.S. Department of Energy under Contract DE-AC03-76SF00098

DISCLAIMER

SPECTROSCOPIC INFORMATION FROM HIGH RESOLUTION IMAGES

R. Gronsky

National Center for Electron Microscopy, Materials and Chemical Sciences Division

Lawrence Berkeley Laboratory, University of California, Berkeley, California 94720 USA.

Phase contrast images recorded under proper conditions of specimen thickness and orientation, as well as microscope alignment, focus and correction of astigmatism, yield a direct indication of atom positions in the sample. Confidence in the interpretation of such images is fostered by comparison with computer simulated images that utilize models of the actual specimen structure and a full account of dynamical scattering. Such images provide the capability for extracting spectroscopic information at the atomic scale. This study critically examines the capabilities and limitations of this technique, including its potential for future development.

1. Introduction

A microscope is, after all, an *imaging* device. The fact that so much modern spectroscopy is done in electron microscopes of the type now commonly known as "analytical electron microscopes"[1] is tribute to their superior spatial resolution. Fine probes can be focused and positioned with precision in the analytical electron microscope (AEM), and the reduced beam spreading in thin samples retains localization during analysis. Yet much of the strength of the AEM as an analytical tool comes from its complementary imaging mode. Images show where the spatially-resolved signals originate, the morphologies of the various constituents responsible for different spectroscopic outputs, and perhaps most importantly, the direct relationship between the sample and the electron probe (its shape, location, etc.). There are few better ways to

evaluate spectroscopic data than to look at an image of the region from which the spectrum was obtained, and in the AEM this assessment occurs in "real time."

Obviously in cases where such microscopy and microanalysis are repetitively performed, the image itself can be all that is needed to evaluate the chemistry of a sample. For example, an experienced microscopist might associate "spectroscopic" information about a specimen with certain image features, as in the identification of a stiochiometrically ordered precipitate phase by its morphology. Unfortunately, this interpretation of an image requires *a priori* knowledge of the sample under study, usually including true spectroscopic data (EDXS, EELS) obtained in an AEM, and is therefore not a routine method for universal application. Furthermore, due to the complex relationship that exists between micrograph contrast and the actual structure of a specimen[2], it is impossible in most cases to deduce any information at all about the number and type of atoms in a microscope sample from simple inspection of its image.

However, it might be possible to extract compositional information about a sample by *detailed* analysis of an image obtained under *carefully-controlled* conditions. When the thickness and orientation of the sample are accurately known, and its image is recorded in a well-characterized microscope, the image can be subjected to comparisons with calculated images, for example, in order to identify its composition. This procedure should in principle work for all imaging modes. Strong diffraction-contrast images are most readily obtained and recognized, and even these may be used in some cases to reveal compositional differences. One technique is to monitor the variation of thickness extinction contour spacings for known wedge-angles in the sample[3], and to relate this variation to composition through the structure factor. Alternatively, phase contrast images are more difficult to obtain, but they provide the best spatial resolution (currently at the atomic level), and therefore the opportunity for spectroscopic analysis on the finest scale.

The purpose of this paper is to critically examine the high resolution phase contrast imaging technique as a method for obtaining such spectroscopic information. Following a review of the technique, examples will be presented to demonstrate its applications for spectroscopic analysis at or near the atomic level.

2. High Resolution Imaging

2.1 Principles of Phase Contrast

Phase contrast in transmission electron microscopy is derived from the variations in phase induced in the incident electron wave by both the specimen and the imaging system. Through proper control of these phase shifts, the exit wave amplitude can be changed at will, yielding wide variations in contrast from the same specimen. Obviously, such contrast is interpretable only if it bears a known relationship to the structure of the specimen, and this occurs only for a limited range of specimen thickness.

Very thin samples behave as "weak phase objects"; their high resolution image contrast is linearly related to the phase shift which they induce in the electron wave and interpretation in terms of their projected atomic potential is relatively straightforward. Thicker specimens induce multiple scattering and attenuation processes that do not preserve any sort of linear relationship between phase shifting of the incident wave and image contrast. The interpretation of their images is considerably more difficult, requiring a full dynamical treatment of the scattering distribution exiting the specimen. These basic concepts are given a detailed description in several good reviews[4-6] , and are highlighted in the following.

Because the phase contrast imaging technique is a multi-beam imaging method (more than one beam are admitted through the objective aperture during imaging), it is necessary to track the phase differences among all imaging beams in order to know their effect on the final image. The contributions are well known.

(i) All Bragg scattering processes induce a phase shift of $-\pi/2$ relative to the forward scattered beam.

(ii) The objective lens induces a further phase shift $\chi(u)$ into all beams at position $\mathbf{u}$ in reciprocal space, where the forward scattered beam is at $\mathbf{u} = 0$. This phase shift is described by

$$\chi(u) = 2\pi/\lambda \{[C_S \lambda^4 u^4] / 4 + [\Delta z \lambda^2 u^2] / 2\} \quad (1)$$

where λ is the wavelength of the illuminating radiation, C_S is the spherical aberration coefficient of the objective lens, and Δz is the extent of defocus of the objective.

Note that at an underfocus setting (Δz negative), the phase shift due to spherical aberration can be compensated, at least in part. This fact was first recognized and described by Scherzer[7] , who specified an optimum defocus setting for phase contrast imaging. Now known as the Scherzer defocus setting, it occurs at

$$\Delta z_{Sch} = - 1.2 (C_S \lambda)^{1/2} \quad (2)$$

and represents the amount of underfocus necessary to pass the greatest number of diffracted beams through the objective lens with nearly identical phase. The actual value of the phase shift induced in this way is $-\pi/2$, which is added to the phase shift due to diffraction ($-\pi/2$) described in (i) above, to yield a total phase shift of $-\pi$. This then is the essence of phase contrast imaging of thin specimens. Those regions of the structure which are responsible for Bragg scattering will be imaged at Scherzer defocus with dark contrast against a light background, since the effect of a $-\pi$ phase shift is a reduction in total wave amplitude of the summed wavefunction at the exit surface of the crystal. At highest resolution, these "regions" are the atoms themselves, represented as their projected potential. Whether or not all atom positions can be imaged is a function of the overall behavior of $\chi(u)$ above.

The resolution limit of a phase contrast image was also recognized by Scherzer[7] , who pointed out that the region of reciprocal space over which $\chi(u)$ is sufficiently well-behaved to produce a uniform phase shift is in fact the region defining the resolution performance of the microscope. The limit of instrumental resolution is set by the largest scattering angle, or equivalently, the largest value of u, which retains a $-\pi/2$ phase shift at the Scherzer defocus value (eq. 2). In real space, this limit is approximately

$$r_{min} = 0.66\, C_s^{1/4} \lambda^{3/4}. \qquad (3)$$

It is emphasized that this description of the principles of phase contrast imaging is strictly limited to very thin specimens that behave as weak phase objects. Thick specimens imaged at the Scherzer defocus setting may not have the same interpretation due to further variations in phase and reductions in amplitude accompanying scattering.

2.2 Experimental Methods

Conventional bright field or dark field transmission electron micrographs are produced by using a small objective aperture to admit only one beam during the image formation process, thereby severely limiting resolution, even in higher voltage microscopes with low C_S values. The image produced in this way is described as having "amplitude contrast". The omission of signal due to obstruction by an objective aperture results in a mapping of the amplitude distribution contained within a single electron wave, the one which goes through the aperture, as the image.

If instead a large objective aperture is used which admits more than one beam during the image formation process, resolution is preserved. The image produced in this way is described as having "phase contrast" because it depends upon the various phase relationships among all beams that go through the aperture. There will be an "amplitude" component for thicker specimens of course, due to those beams multiply-scattered through large enough angles to be stopped by the (finite) aperture, or the lens bore itself, but this will usually be a relatively low resolution component. High resolution detail will also be reduced through the loss of those singly-scattered beams stopped by the aperture or the lens bore, even for thin specimens, but an equally damaging effect comes from any perturbation in the phase of the imaging beams which prevents them from contributing useful information to the image.

For these reasons there is an optimum objective aperture size, set by the instrumental resolution limit of the microscope. The aperture chosen in this way acts to increase signal-to-

noise by removing unwanted background from the image. It is possible to produce phase contrast images through larger objective apertures of course, but their interpretation requires more attention to the phase aberrations beyond the Scherzer limit, usually through extensive computer simulations[8].

Once the microscope has been properly fitted with usable objective apertures, it must be further optimized before high resolution imaging. Alignment of both the microscope and specimen is critical during this stage, followed by the adjustment of beam brightness and coherence (both spatial and temporal), astigmatism, and finally focus, as described fully in references (5) and (6). It is emphasized that intuitive notions of sharpness associated with proper focus are inappropriate for phase contrast images. While it is true that images will appear sharp in the absence of astigmatism, they may do so over a rather large deviation from the Scherzer defocus condition. Actually the only tangible focus setting during phase contrast imaging is the minimum contrast condition, also called the "dark field focus" condition in scanning transmission electron microscopy [4] , which occurs at a defocus value of

$$\Delta z_{MC} = -0.44\,(C_S\lambda)^{1/2} \qquad (4)$$

and maintains a near zero phase shift for the largest number of scattered beams. It is tangible because it is recognized by the microscopist at a setting of focus for which all background phase granule contrast in the transmission image becomes a true minimum; overfocus or underfocus beyond Δz_{MC} clearly increases contrast. From this position all focus settings, including the most important Δz_{Sch}, are quantitatively accessible, with uncertainties taken up by a "through-focus" series.

Of singular importance in the interpretation of phase contrast images is the quality of the specimen, which in addition to meeting the constraints on thickness described above, must also be clean, flat, and preferably decreasing monotonically to zero thickness at a free-standing edge. The last of these affords the opportunity to test the thickness dependence of the image, and

ensure its "representative" nature.

As a final component to all modern high resolution phase contrast imaging studies, image simulation and processing play a role of ever-increasing importance. The simulation of images follows closely the sequence of events in the microscope, coupling a calculation of the interaction between the incident beam and the specimen with a calculation of the effects of the electron-optical system. The former usually embodies the physical optics description of Cowley and Moodie[9,10], in the multislice formulation, while the latter usually adopts the form of information theory[11]. Such simulations are then used to design high resolution imaging experiments, to test the feasibility of being able to image specific atomic structures, and to interpret experimental results, often at levels of resolution which exceed instrumental performance[12]. Image processing techniques, including digital methods commonly used in the field of optics[13,14] , have also been applied to high resolution electron microscopy, with particular attention to the phase contrast methods described in this article[15]. These will show their greatest benefit when performed on-line[16] , and in "real-time".

3. Applications to Compositional Analyses

3.1 Identification of Ordered Precipitates

One of the most straightforward applications of the phase contrast imaging technique for compositional analysis is the study of long-range-ordered precipitate phases residing within a well-characterized, disordered, matrix phase. The matrix serves as a reference against which conclusions can be drawn regarding the precipitate phase. The example shown in Fig. 1 is a spherical, 10 nm diameter, fully-ordered precipitate of the δ' phase, Al_3Li, in a dilute binary alloy, such that the matrix α phase is essentially pure Al. Due to the $L1_2$ structure of the δ' phase and its parallel orientation relationship with the α phase, the precipitate is identified by the spacing of its superlattice which is fully coherent with the matrix. Although it appears as though this can be done by simple inspection for all such cases, it is cautioned that the image is sensitive

to not only thickness and defocus as described above, but also the position of the precipitate within the total depth of the sample[17] . Image simulation is therefore required before reaching a confident interpretation of the phase contrast associated with different compositions or the degree of order[18] of the precipitate phase. Calculations have also shown that this problem increases in complexity at higher resolution[19] .

3.2 Detection of Composition Gradients

There have been a number of attempts to associate detectable changes in lattice fringe spacing with variations in composition in both metallic[20, 21] and ceramic[22] alloy systems. The working hypothesis here is that if the lattice parameter of a material changes with composition, and if the phase contrast image faithfully reproduces the local lattice spacings in the sample, then it should be possible to measure composition gradients at the atomic plane level by measurement of lattice fringe spacings in the image. Unfortunately in this case the level of experimental complexity is again increased. Not only must all phase contrast conditions be rigidly monitored for this method to succeed[23, 24], but there must also be further knowledge of the specific dependence of lattice parameter on composition for any interpretation to be acceptable. A simple assumption of Vegard's law (a linear interpolation between the lattice parameters of the constituent components) can be grossly in error; the gold-nickel alloy system studied first in ref. 20 by lattice imaging is a case in point, having a very strong positive deviation from Vegard's law [25] .

Nevertheless the technique offers an attractive alternative for very high spatial resolution microanalysis, as illustrated in the next two figures. Figure 2 shows a phase contrast image of a grain boundary precipitate in an Al-9.5 at % Zn alloy aged for 30 mins. at 180° C. The boxed region in (a) is enlarged in (b) to show the lattice fringes of the contiguous phases subjected to careful measurements. The average interplanar spacings of the well-developed particle agrees well with prior x-ray results [26] , while the use of an internal magnification standard (the spacing of the lattice fringes in the Al matrix phase) permits equivalent accuracy in

considerably more localized regions. Measurements were performed by recording the average spacing of ten-fringe groups, advancing by approximately one fringe width normal to the grain boundary at each measurement. The results, plotted within the error bars of each measurement, are shown in Fig. 3 where the decreased fringe spacing is suggestive of solute depletion as the boundary is approached from either matrix or precipitate side. Regardless of the interpretation, it is significant that lattice parameter variations of only 1.28% can be detected within a nanometer of the boundary plane. However it is emphasized that the interpretation of particularly these slowly-varying interfringe spacings requires careful consideration of the specimen and electron-optical parameters outlined above.

3.3 Identification of Boundary Layers and Interfacial Films

Abrupt variations in phase contrast are another matter, and these can clearly and accurately signal the presence of very small amounts of a new phase, even leading to its quantitative identification in the absence of any other spectroscopic information. Two examples follow.

During a study of the formation and degradation of $Cu_{2-x}S/CdS$ single-crystal heterojunctions[27] , it was discovered that poor photovoltaic performance could be associated with the presence of a thin (<20 nm) interfacial phase sandwiched between the low chalcocite (Lch) absorber layer and the CdS substrate. Figure 4 shows the phase contrast image that led to the identification of this film as a high temperature polymorph with tetragonal structure. This intermediate phase was inhibited from formation during growth on all interfaces (a) except those (b) in basal CdS orientation, also verified by the compositional information in these high resolution images.

Discontinuous structures on an even finer scale can be identified by the same technique, as revealed in Fig. 5. This phase contrast image of the interface between GaAs and its thermal oxide, γ-Ga_2O_3, shows that as Ga is consumed during oxide growth, the As released by the

reaction accumulates in the form of small (5 nm) hexagonal precipitates. Their protrusion into the GaAs substrate suggests that the elemental As particles are nucleated by locally high losses of Ga from the substrate, resulting in the local collapse of the GaAs lattice[28] .

3.4 Detection of Atomic Columns

Obviously the fullest exploitation of phase contrast imaging for spectroscopic analysis comes at the ultimate resolution performance of the transmission electron microscope, when atomic columns are resolved. In order to more carefully explore the practical limitations of this technique, a computer simulation study was conducted [29] on the visibility of substitutional impurities in an otherwise perfect silicon crystal. The impurities were arranged in columns along the beam direction, a <110> direction in the Si lattice, at various concentrations. Images were calculated using the instrumental parameters for the JEOL JEM 200CX equipped with ultrahigh resolution goniometer stage, namely a C_S of 1.2 mm, half-width spread in defocus of 5nm, and beam convergence half-angle of 1 milliradian. Results for As atoms in silicon are presented here.

Figure 6 is a comparison of images to illustrate their thickness variation. The As concentration in the arrowed column is identically 50% in each case, and all imaging conditions are the same throughout, yet there is a clear difference in detectability. The impurity column is only strongly observable when the specimen thickness exceeds one half of the effective extinction distance (ξ_{111} = 28.8 nm), or 14.4 nm.

Defocus variation is shown in Fig. 7 for a 10% As column in a 28.8 nm thick specimen. Note that the impurity column appears more visible at 10 nm underfocus, even though the spatial resolution of the image is optimized at 66 nm underfocus (Δz_{Sch}), and that the relative contrast of the impurity column is reversed in both cases. This figure demonstrates the dramatically sensitive response of high resolution phase contrast images to even slight changes in focus, highlighting once again the caution that must be exercised in accurately determining all experimental parameters before quantitative interpretation can be attempted.

Figure 8 suggests a lower limit of detectability for this study. At constant thickness (28.8 nm) and defocus (-66nm), a column of Si atoms replaced with one containing only 5% As is on the threshold of detection, while the 20% As column is quite obviously detectable. However, at threshold, other effects begin to dominate image character. One source of image artefacts that cannot be ignored in thin specimens is the surface, particularly in the case of silicon when native oxide overlayers are present. This effect was examined in another study[30] , and shown in Fig. 9. By superimposing a 1.57 nm thick amorphous silica on both the top and bottom surfaces of a <110> oriented Si crystal (otherwise perfect), isolated changes in atomic column contrast are observed (see arrows). The effect is especially pronounced in a very thin specimen (2.3 nm in (a)), but quickly subsides when the total thickness of the specimen equals the combined thickness of the oxide film (b). Nevertheless, note that there is very little difference in image contrast between the As-containing column in Fig. 8(a) and the oxide-affected column in Fig. 9(a).

3.5 Identification of Atomic Species

As a final example of the potential of this technique, the capabilities of the Atomic Resolution Microscope[31, 32] for atomic identification are illustrated. Previous experimental images of cubic $BaTiO_3$ showed contrast which was interpreted on the basis of comparisons with simulated images to be indicative of the difference in ionic species distributed as columns through the structure[32] along the beam direction. This is a significant result, since it represents the highest spatial resolution for identification of anions in electron microscope samples. To extend this study, the following simulations were performed, using relevant parameters for the ARM, i.e., 1000 kV, Cs of 2.6 mm, half-width spread in defocus of 10nm, and beam convergence half-angle of 0.2 milliradian.

Figure 10 shows the anticipated image of a 4nm thick sample oriented along a cube axis at 60 nm underfocus (near Δz_{Sch}) recorded in the ARM. The only difference between the two

samples is that (a) contains oxygen anions in normal face-centered locations while (b) has no oxygen at all. Note that there is a clear distinction between these images, recorded at optimum defocus. Unfortunately this distinction can, other other less controlled conditions, be completely obscured, as the images in Fig. 11 demonstrate. Figure 11(a) simulates a micrograph of a $BaTiO_3$ sample 8nm thick at 90nm underfocus, while Fig 11(b) is the same structure without oxygen, 160nm thick at 75nm underfocus. Note that except for a change in overall contrast levels, these images are identical, making it impossible to identify anions in the structure under *arbitrary* imaging conditions. The implication here is that the microscopist must take proper care to both choose and document all experimental conditions in order to extract spectroscopic information from phase contrast images at the atomic level.

4. Conclusions

The phase contrast imaging technique of high resolution electron microscopy is an extremely sensitive probe of atomic structure in thin samples. As such it provides the capability for performing spectroscopic analysis by relating local changes in contrast or lattice fringe spacing to local changes in composition within the sample, and in special cases to the detection of even a few atoms of an impurity element within a single column of atoms parallel to the electron beam. This type of analysis can never be done naively however; phase contrast images are also sensitively affected by slight variations in specimen thickness, the presence of contamination overlayers, the quality of beam alignment and coherence, and of course the focus setting of the objective lens. The key to successful application of the method lies in comparing experimental images obtained over a wide range of experimental conditions to computer simulations which assume various structural models. Imaging matching selects the correct model, accurate to atomic dimensions. It is clear that with future developments in on-line digital acquisition and processing of phase contrast images, atomic resolution spectroscopy in the transmission electron microscope will become possible.

Acknowledgements

The author extends his gratitude to the organizers for their invitation to present this review. The assistance of Dr. M.A. O'Keefe and SHRLI for the simulations in Figure 11 are also gratefully acknowledged.

This work is supported by the Director, Office of Energy Research, Office of Basic Energy Sciences, Materials Science Division of the U.S. Department of Energy under Contract No. DE-AC03-76SF00098.

References

[1] Introduction to Analytical Electron Microscopy, J.J. Hren, J.I. Goldstein and D.C. Joy (eds.), Plenum Press, N.Y. (1979).

[2] R.C. Valentine, in: Advances in Optical and Electron Microscopy, Vol.1, R. Barer and V.E. Coslett (eds.), Academic Press, London (1966), p. 180.

[3] H. Kakibayashi and F. Nagata, Jpn. J. Appl. Phys. **24**, L905 (1985).

[4] J.M. Cowley, Diffraction Physics (2nd edition), North Holland, N.Y. (1981).

[5] J.C.H. Spence, Experimental High-Resolution Electron Microscopy, Clarendon Press, Oxford (1981).

[6] R. Gronsky, in: Treatise on Materials Science and Technology: Experimental Techniques, Vol. 19B, H. Herman (ed.), Academic Press, N.Y. (1983) p. 225.

[7] O. Scherzer, J. Appl. Phys. **20**, 20 (1949).

[8] M.A. O'Keefe, P.R. Buseck and S. Iijima, Nature **274**, 322 (1978).

[9] J.M. Cowley and A.F. Moodie, Acta Cryst. **10**, 609 (1957).

[10] J.M. Cowley and A.F. Moodie, Acta Cryst. **12**, 353 (1959).

[11] F.A. Lenz, in: Electron Microscopy in Materials Science, U. Valdrè (ed.), Academic Press, N.Y. (1971) p. 541.

[12] M.A. O'Keefe, in: Electron Optical Systems, J. Hren, F.A. Levy, E. Munro and P.B. Sewell (eds.), SEM, Inc., AMF O'Hare, IL (1984) p. 209.

[13] H.C. Andrews, Computer Techniques in Image Processing, Academic Press, New York, 1970.

[14] A. Rosenfeld and A.C. Kak, Digital Picture Processing, Second Edition, Volumes 1 and 2, Academic Press, New York, 1982.

[15] W.O. Saxton, Computer Techniques for Image Processing in Electron Microscopy, Advances in Electronics and Electron Physics, Supplement 10, L. Marton (ed.), Academic Press, New York, 1978.

[16] E.D. Boyes, B.J. Muggridge and M.J. Goringe, J. Microscopy **127**, 321 (1982).

[17] R. Sinclair, K. Schneider and G. Thomas, Acta Met. **23**, 873 (1975).

[18] J. Dutkiewicz and G. Thomas, Thin Solid Films **32**, 329 (1976).

[19] J.M. Howe and R. Gronsky, in: Proc. 44th Ann. Meeting Elec. Mic. Soc. Amer. G.W. Bailey (ed.), San Francisco Press, San Francisco (1986) p. 828.

[20] R. Gronsky, M. Okada, R. Sinclair and G. Thomas, in: Proc. 33rd Ann. Meeting Elec. Mic. Soc. Amer. G.W. Bailey (ed.), Claitor's, Baton Rouge, La. (1975) p. 22.

[21] R. Gronsky and G. Thomas, in: Proc. 35th Ann. Meeting Elec. Mic. Soc. Amer. G.W. Bailey (ed.), Claitor's, Baton Rouge, La. (1977) p. 116.

[22] D.R. Clarke, Ultramicroscopy **4**, 33 (1979).

[23] J.C.H. Spence, J.M. Cowley and R. Gronsky, Ultramicroscopy **4**, 429 (1979).

[24] D.J.H. Cockayne and R. Gronsky, Phil. Mag. **A 44**, 159 (1981).

[25] C.E.C. Ellwood and K.Q. Bagley, J. Inst. Metals **80**, 617 (1952).

[26] M. Simerska and V. Synecek, Acta Met. **15**, 223 (1967).

[27] T. Sands, J. Washburn and R. Gronsky, Solar Energy Materials **10**, 349 (1984).

[28] T. Sands, J. Washburn and R. Gronsky, Materials Letters **3**, 247 (1985).

[29] J.H. Rose, Ph.D. Thesis, University of California, LBL - 20381, September, 1985.

[30] R. Kilaas and R. Gronsky, Ultramicroscopy **16**, 193 (1985).

[31] R. Gronsky, Mat. Res. Soc. Symp. Proc. Vol. 31, W. Krakow, D. Smith and L.W. Hobbs (eds.), Elsevier, New York (1984) p. 1.

[32] R. Gronsky, in: Proc. 42nd Ann. Meeting Elec. Mic. Soc. Amer. G.W. Bailey (ed.), San Francisco Press, San Francisco (1984) p. 368.

Figure Captions

Fig. 1. Lattice image of a 10nm diameter, fully ordered, precipitate (large arrow) of the δ' phase Al3Li in a dilute binary alloy. The matrix phase (α) is disordered and essentially pure Al. Although the two phases are perfectly coherent, the interface (small arrows) can be located by the change in fringe spacing.

Fig. 2. Lattice image of a grain boundary precipitate in an Al-9.5at%Zn alloy (a), with boxed region enlarged in (b). The lattice fringes within the precipitate (left) and matrix (right) were carefully measured for changes in spacing as the boundary is approached. Data are plotted in Fig. 3.

Fig. 3 Plot of fringe spacing vs distance across the grain boundary shown in Fig. 2. Measurements were averaged over 10-fringe groups, with error bars showing the variation, and the decreased spacing as the boundary is approached from either side is suggestive of solute depletion. In this case, a 1.28% change in lattice parameter is detected within one nanometer of the boundary plane.

Fig. 4 Phase contrast image of two heterojunctions between single crystal CdS (bottom) and Cu2-xS, in its low chalcocite (Lch.) modification (top). All interfaces were characterized by a smooth structural transition between absorber and collector layers (a) except those grown on CdS in basal orientation on the Cd face (b). Here the detrimental transition layer of tetragonal phase (Tet.) which is responsible for photovoltaic breakdown is revealed at less than 20 nm thickness.

Fig. 5 Phase contrast image of the interface between GaAs and its thermal oxide, γ-Ga2O3, showing the presence of elemental As accumulation in 5nm particle form.

Fig.6 Simulated images for the JEOL JEM 200CX electron microscope showing contrast variations of an As impurity column in Si along a <110> orientation. The arrowed column contains 50% As, and the specimen thickness varies as (a) 5nm, (b) 10nm, (c) 21.9nm, and (d) 28.8nm, all at the same defocus value (Δz_{Sch}). The impurity column is only strongly observable when the specimen thickness exceeds one half of the effective extinction distance (ξ_{111} = 28.8nm).

Fig. 7 Simulated images for the JEOL JEM 200CX electron microscope showing contrast variations of a 10% As impurity column in a Si sample of 28.8nm thickness at (a) 10nm underfocus and (b) 66nm underfocus (Δz_{Sch}), also in <110> orientation. Note that the arrowed impurity column is more visible away from the optimum focus setting for best resolution.

Fig. 8 Simulated images for the JEOL JEM 200CX electron microscope showing contrast variations of As impurities in a sample of Si in <110> orientation, 28.8nm thick, at Scherzer defocus (-66nm). The arrowed column containing only 5% As is on the threshold of detection in (a) while the 20% column is clearly detectable in (b).

Fig. 9 Comparison of simulated images for the JEOL JEM 200CX electron microscope showing how the presence of a thin (1.57nm) overlayer of amorphous silica can affect the contrast of isolated columns (arrowed) in a pure <110> oriented Si sample. The effect is most noticeable in thin samples (2.3nm in (a)), but rapidly diminishes when the thickness of the silica film is less than the thickness of the silicon substrate (b).

Fig.10 Comparison of images simulated for the ARM[31] showing BaTiO3 in <001> projection, 4nm thick, 60nm underfocus. The sample in (a) contains oxygen in its proper location, while (b) contains no oxygen. Contrast is distinctively different in both cases.

Fig. 11 Comparison of images simulated for the ARM[31] showing BaTiO3 in <001> projection, (a) with and (b) without oxygen in the structure. These images look the same because of a difference is both thickness and defocus between them.

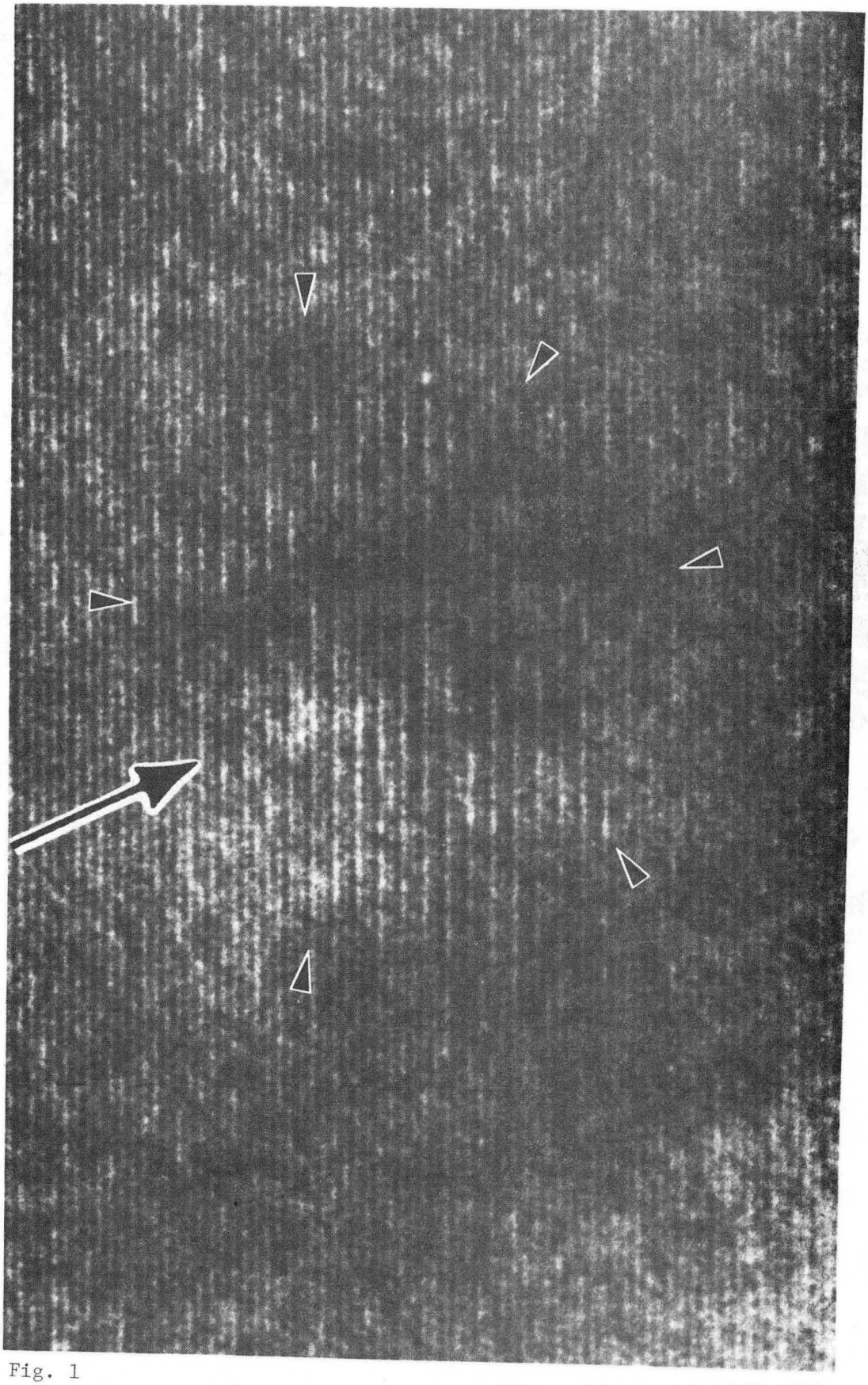

Fig. 1

XBB 868-6071

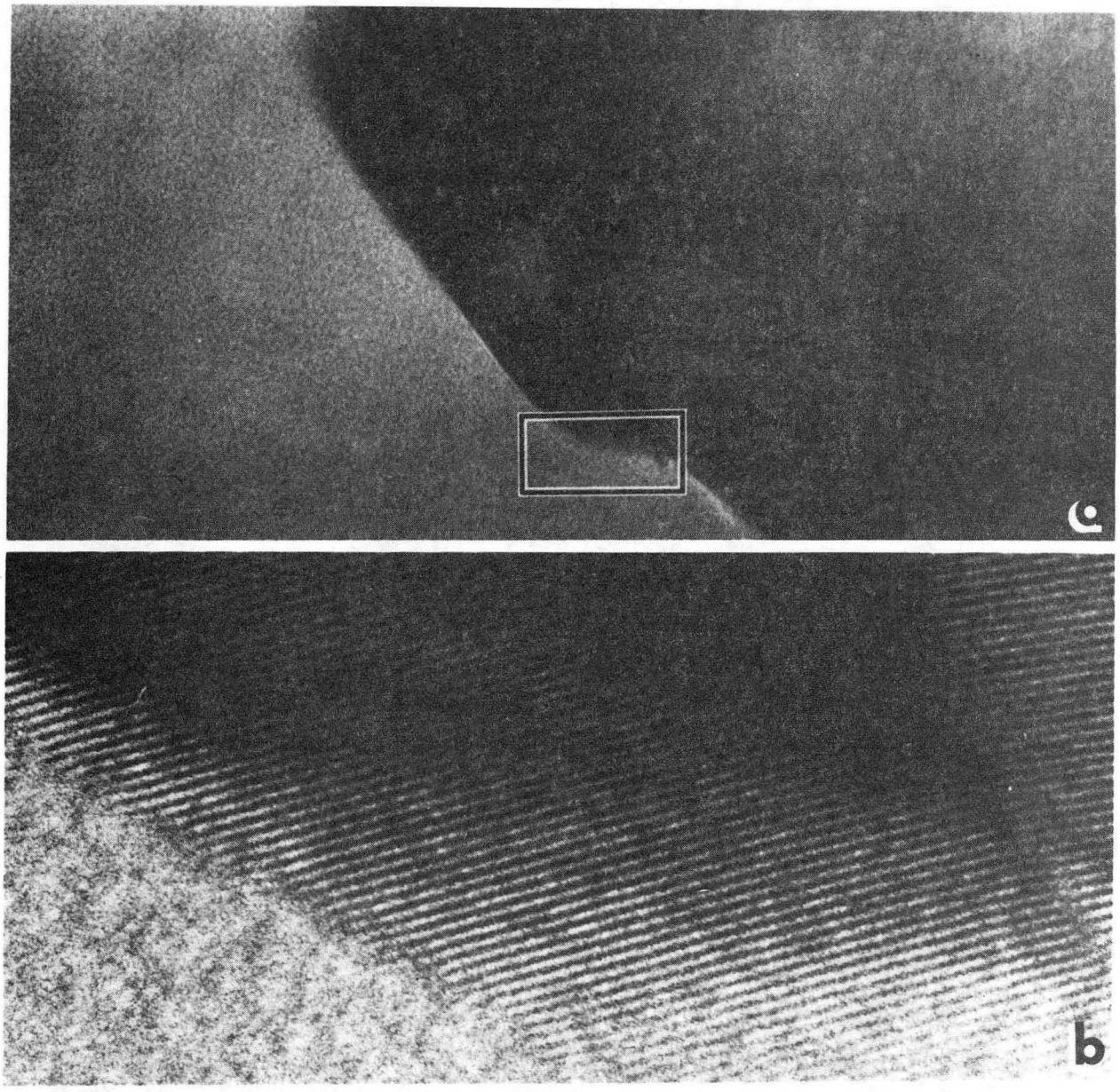

Fig. 2

XBB 868-6072

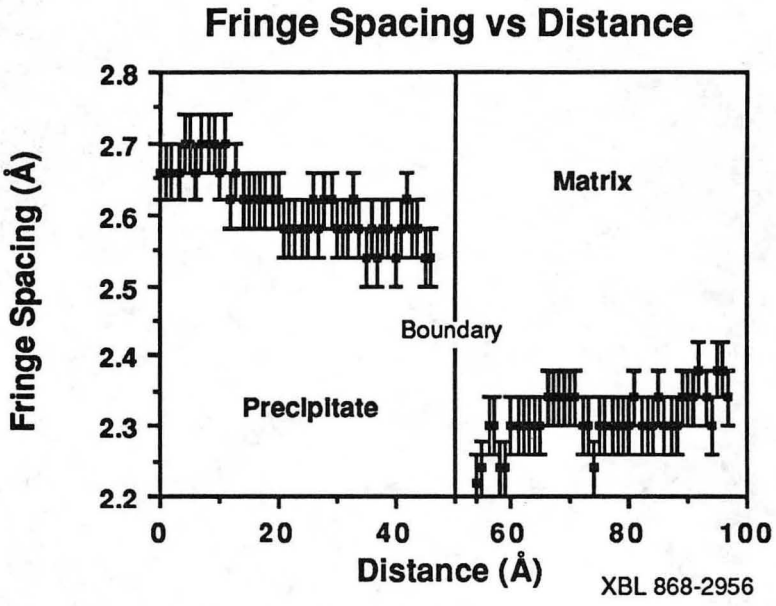
Fringe Spacing vs Distance
Fringe Spacing (Å)
2.8
2.7
2.6
2.5
2.4
2.3
2.2
0
20
40
60
80
100
Distance (Å)
Matrix
Boundary
Precipitate
XBL 868-2956

Fig. 3

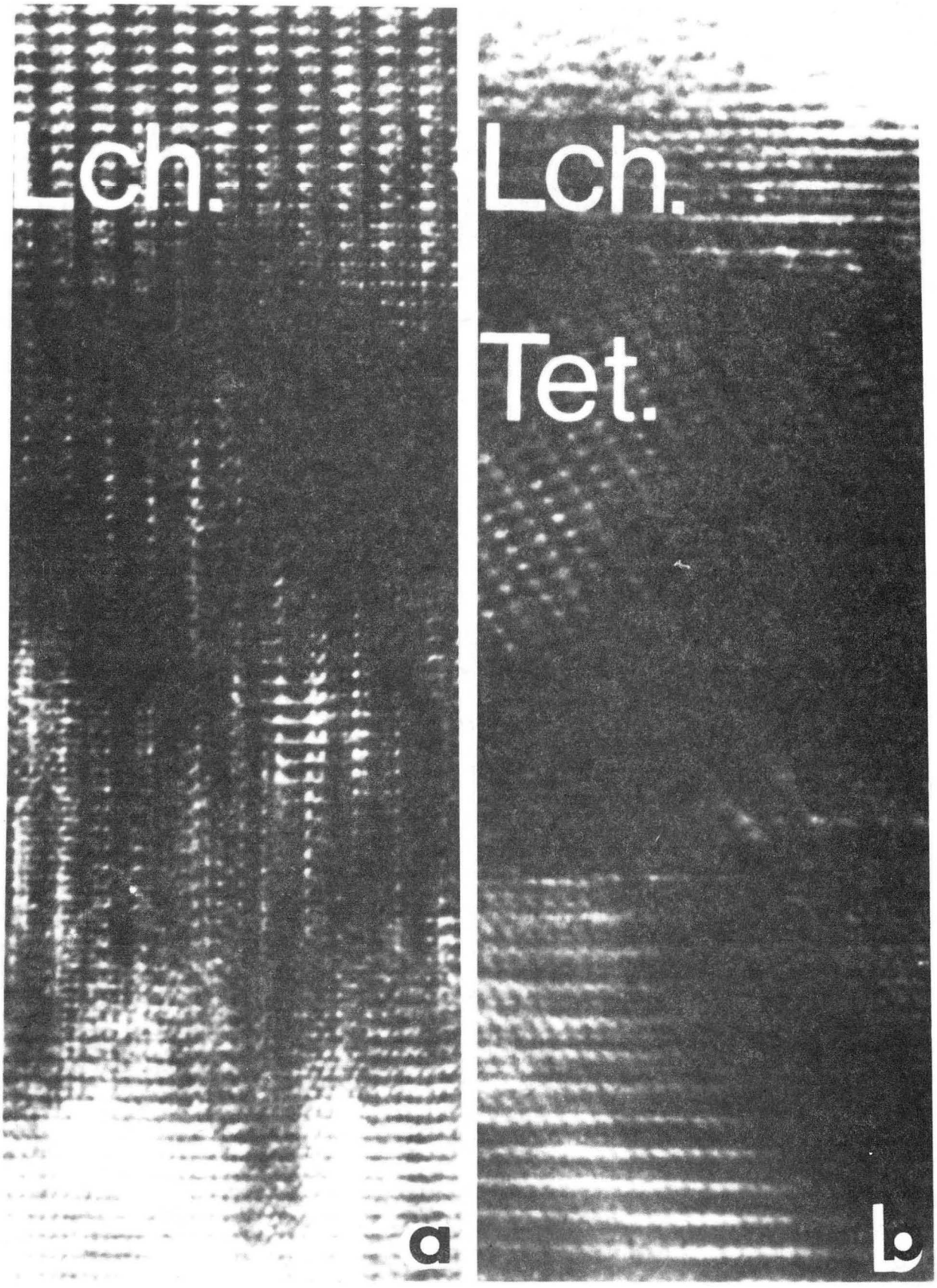

Fig. 4

XBB 868-6070

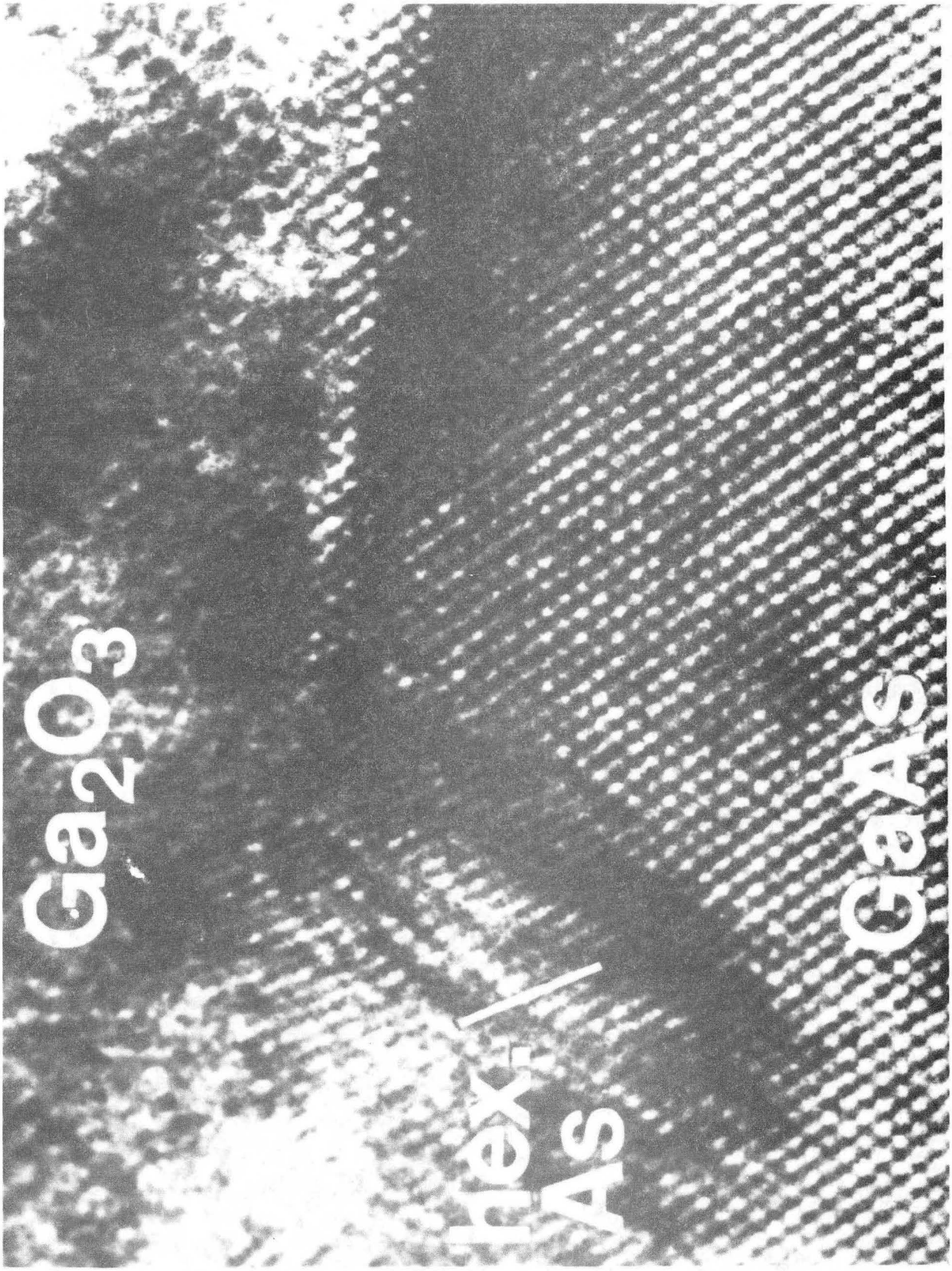

XBB 868-6069

Fig. 5

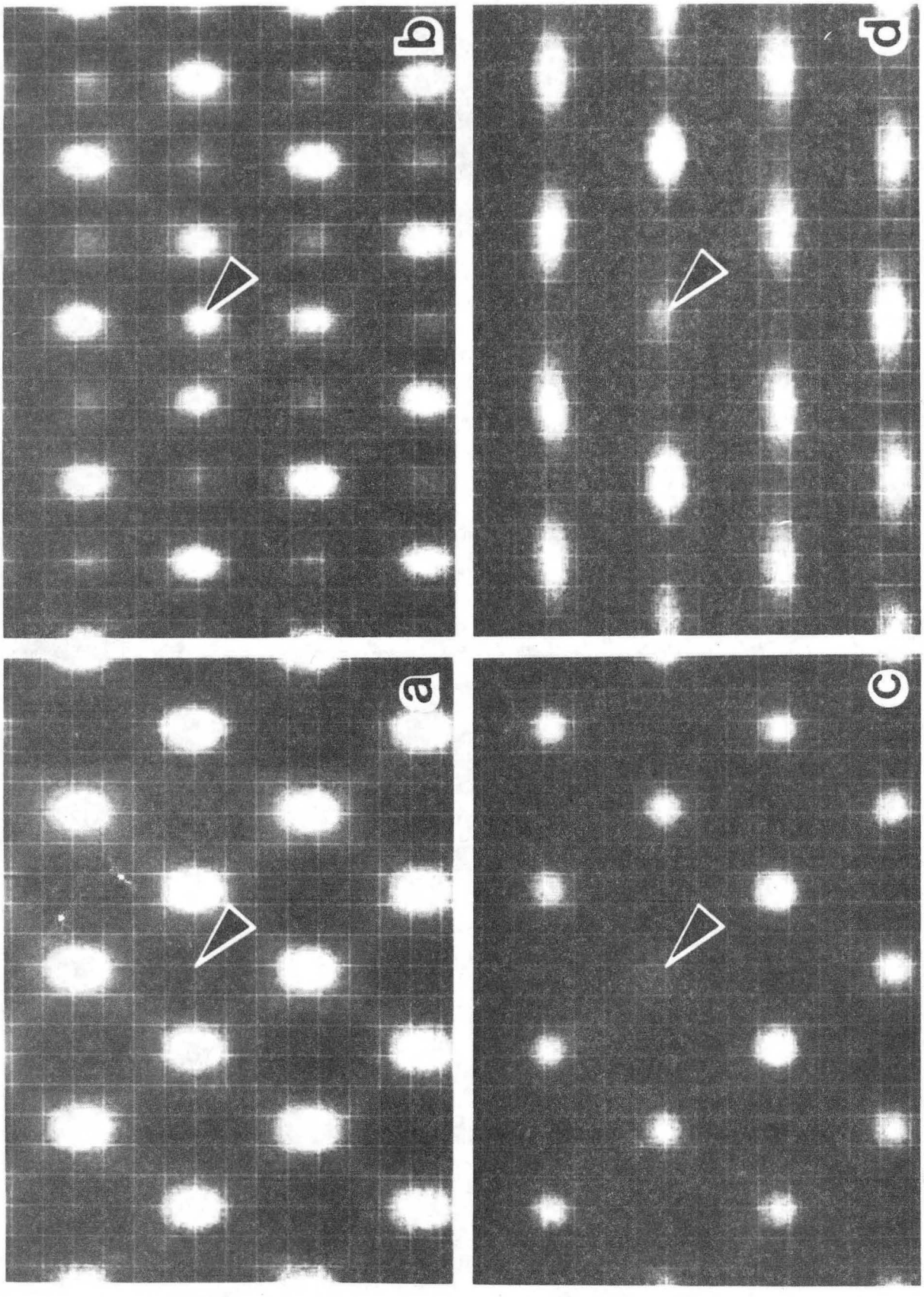

XBB 868-6066

Fig. 6

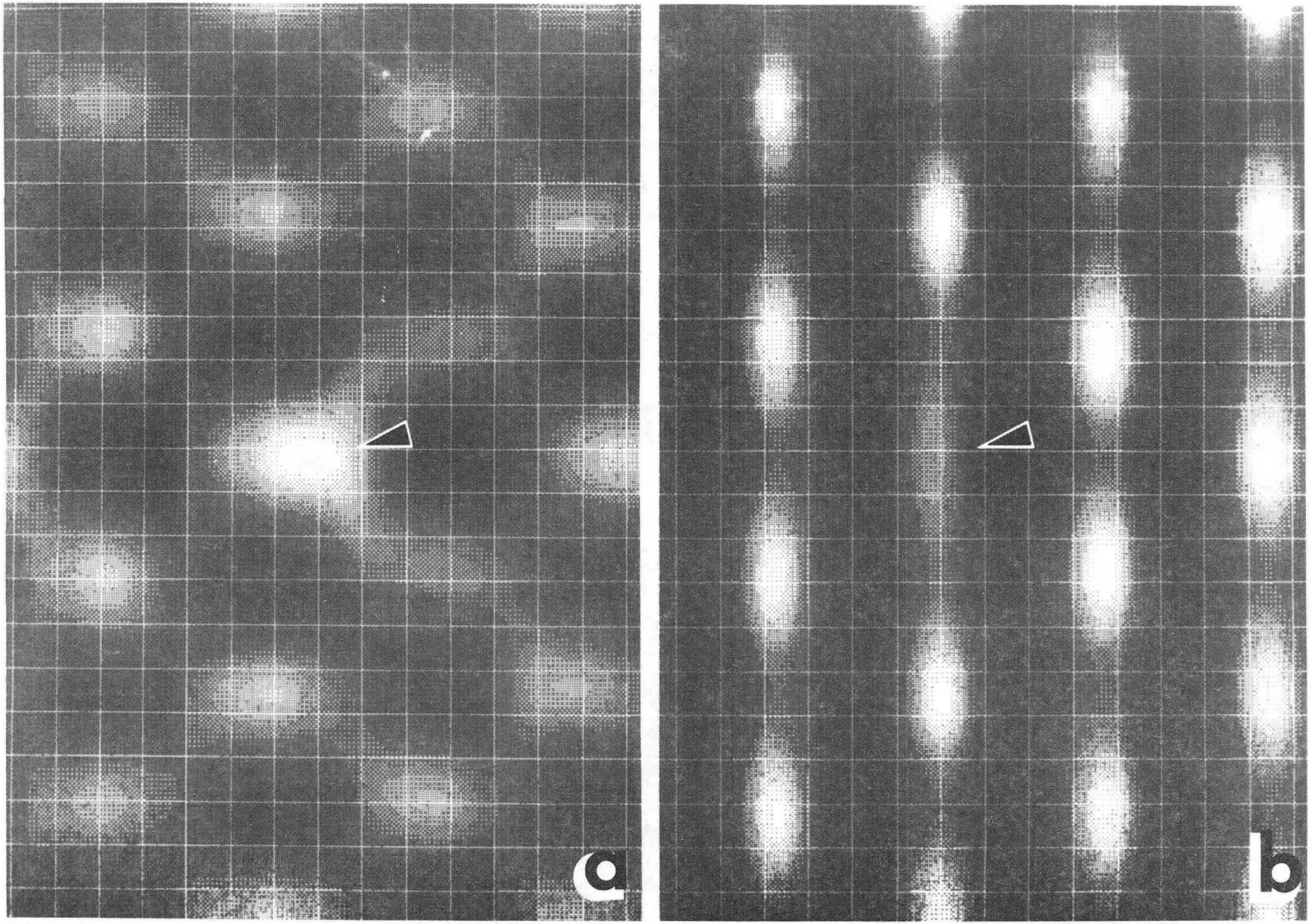

Fig. 7

XBB 868-6068

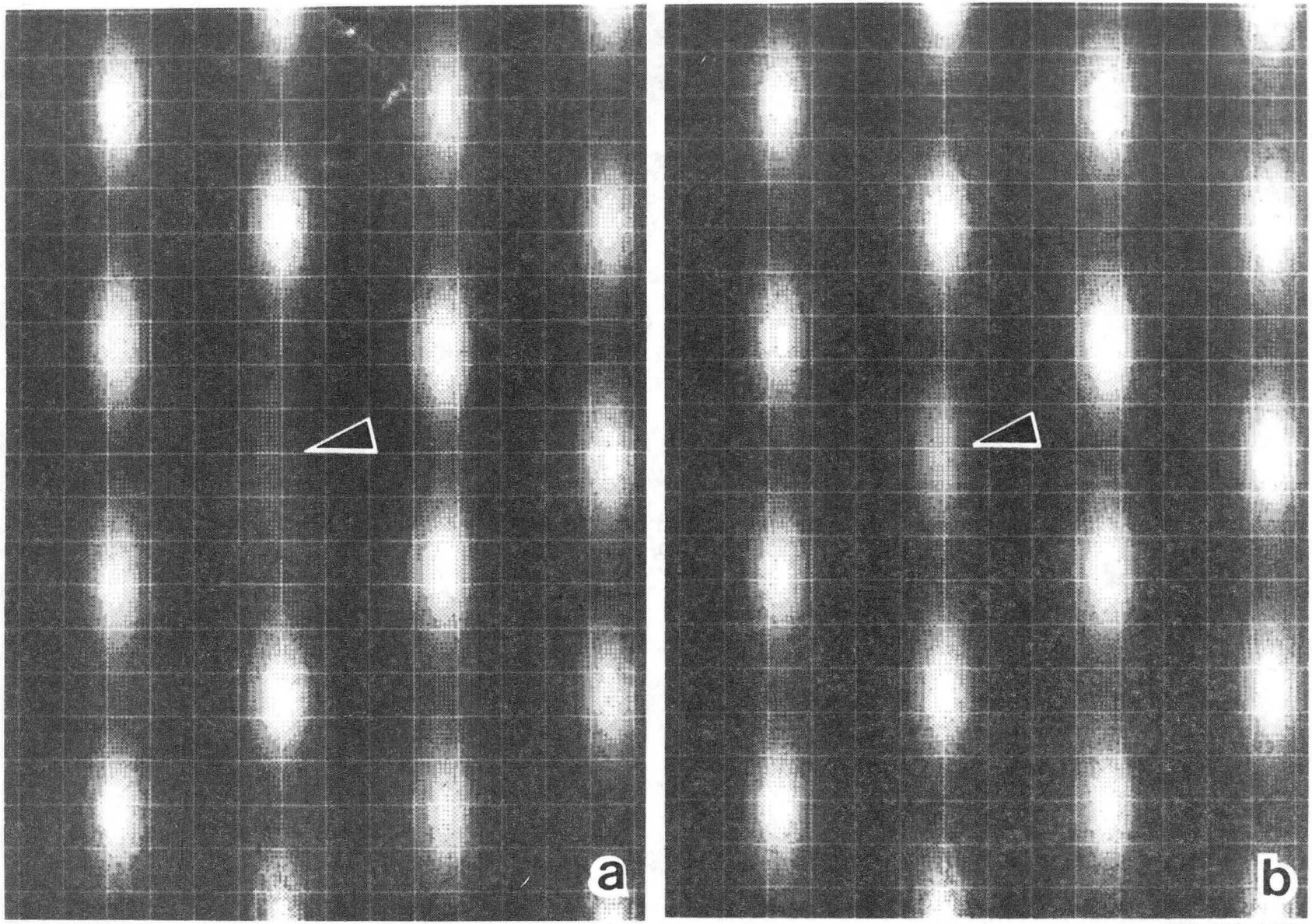

Fig. 8

XBB 868-6067

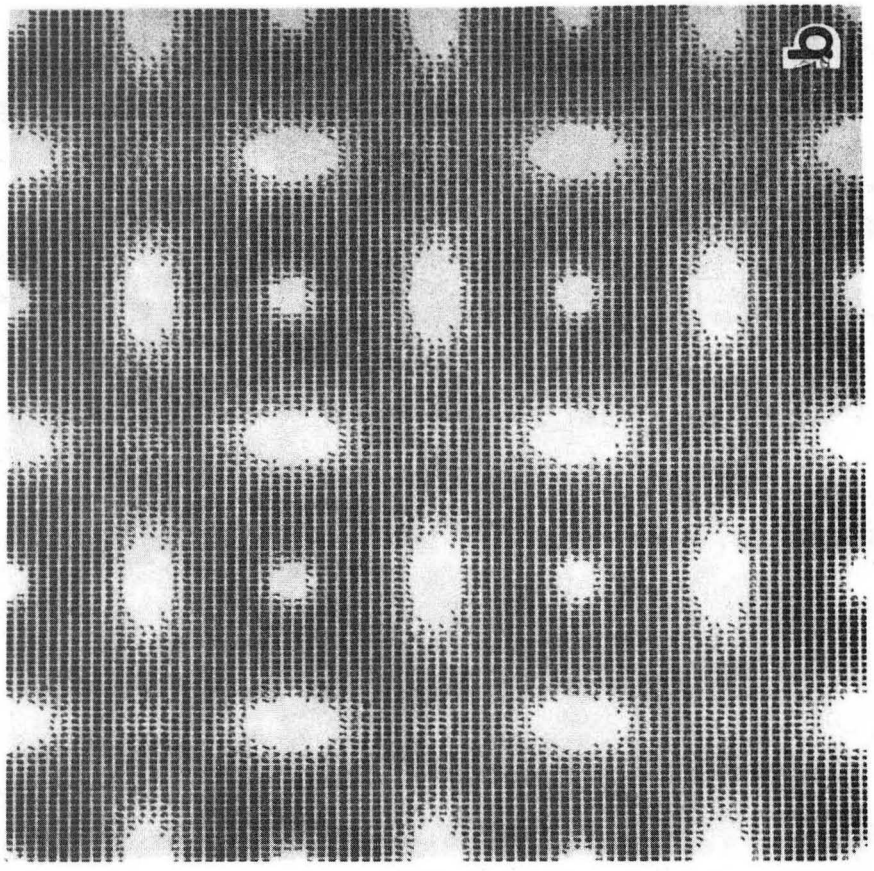

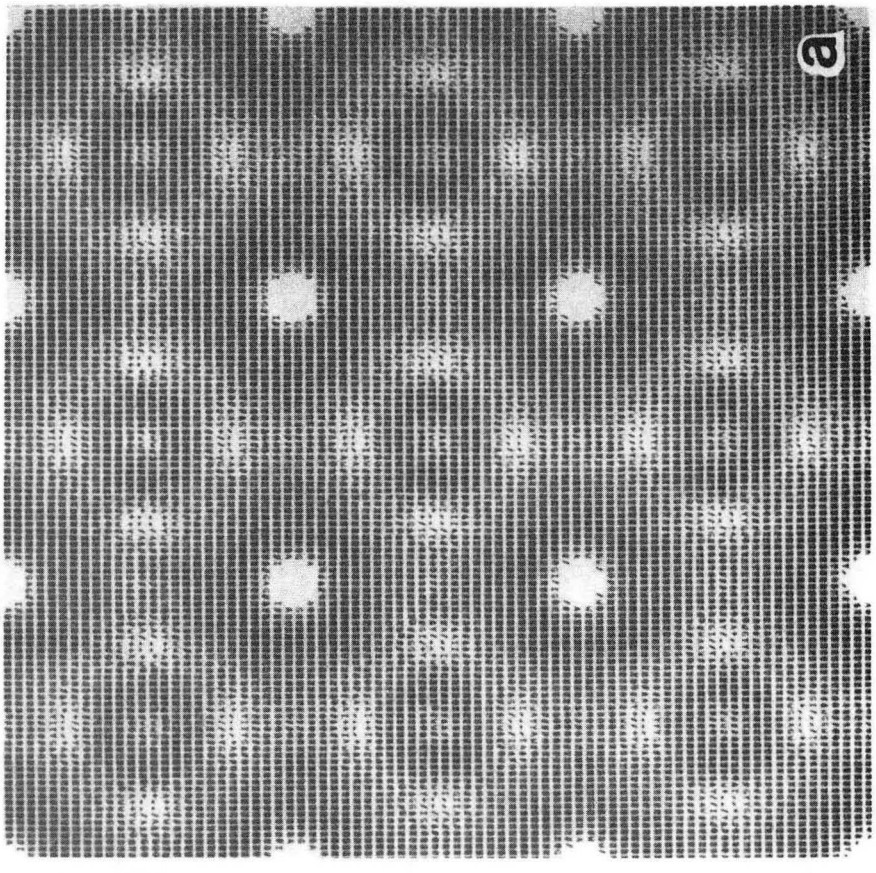

XBB 868-6073

Fig. 10

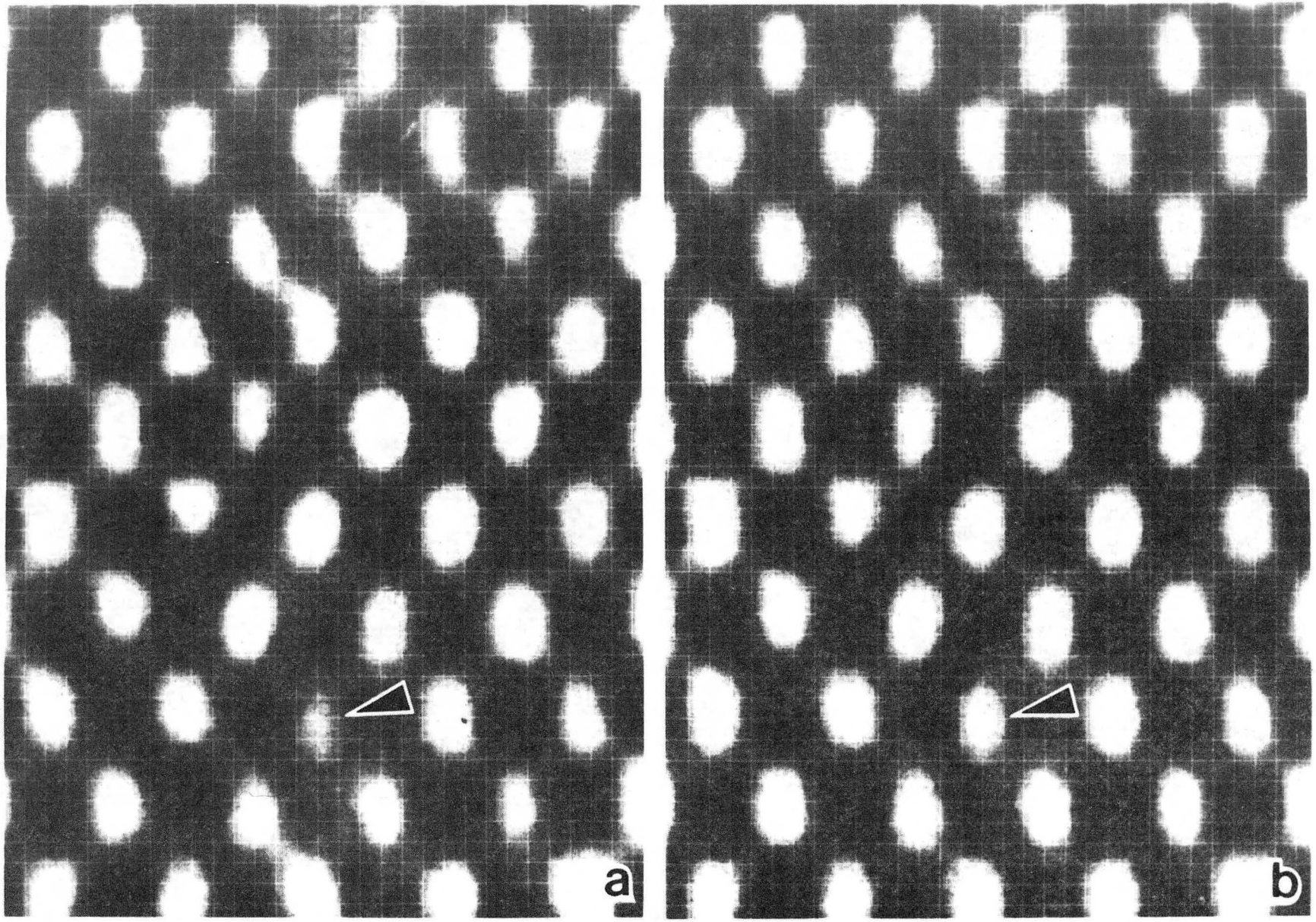

Fig. 9

XBB 868-6065

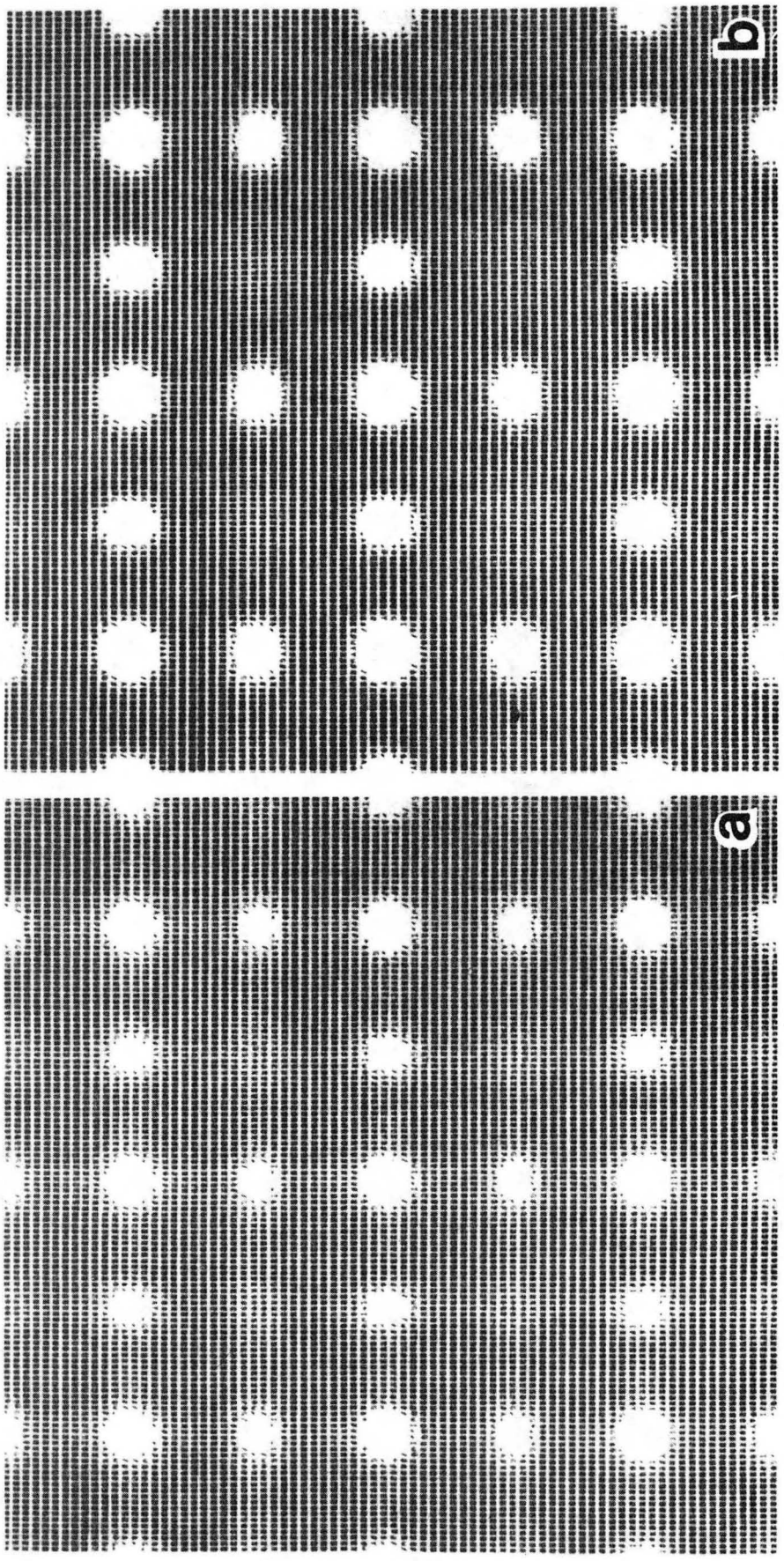

XBB 868-6064

Fig. 11

LAWRENCE BERKELEY LABORATORY
TECHNICAL INFORMATION DEPARTMENT
UNIVERSITY OF CALIFORNIA
BERKELEY, CALIFORNIA 94720